






SpiDR: A Reconfigurable Digital Compute-in-Memory Spiking Neural Network Accelerator for Event-based Perception

Deepika Sharma , Graduate Student Member, IEEE, Shubham Negi , Graduate Student Member, IEEE, Trishit Dutta , Member, IEEE, Amogh Agrawal , Member, IEEE, and Kaushik Roy , Fellow, IEEE,

arXiv:2411.02854v1 [cs.AR] 5 Nov 2024

Abstract—Spiking Neural Networks (SNNs), with their inherent recurrence, offer an efficient method for processing the asynchronous temporal data generated by Dynamic Vision Sensors (DVS), making them well-suited for event-based vision applications. However, existing SNN accelerators suffer from limitations in adaptability to diverse neuron models, bit precisions and network sizes, inefficient membrane potential (Vmem) handling, and limited sparse optimizations. In response to these challenges, we propose a scalable and reconfigurable digital compute-in-memory (CIM) SNN accelerator SpiDR with a set of key features: 1) It uses in-memory computations and reconfigurable operating modes to minimize data movement associated with weight and Vmem data structures while efficiently adapting to different workloads. 2) It supports multiple weight/Vmem bit precision values, enabling a trade-off between accuracy and energy efficiency and enhancing adaptability to diverse application demands. 3) A zero-skipping mechanism for sparse inputs significantly reduces energy usage by leveraging the inherent sparsity of spikes without introducing high overheads for low sparsity. 4) Finally, the asynchronous handshaking mechanism maintains the computational efficiency of the pipeline for variable execution times of different computation units. We fabricated SpiDR in 65 nm Taiwan Semiconductor Manufacturing Company (TSMC) low-power (LP) technology. It demonstrates competitive performance (scaled to the same technology node) to other digital SNN accelerators proposed in the recent literature and supports advanced reconfigurability. It achieves up to 5 TOPS/W energy efficiency at 95% input sparsity with 4-bit weights and 7-bit Vmem precision.

Index Terms—Dynamic Vision Sensors (DVS), compute-in-memory (CIM), spiking neural networks (SNNs), optical flow estimation, event-based vision.

I. INTRODUCTION

In the evolving landscape of machine vision, dynamic vision sensors (DVS) [1], [2] have emerged as a unique visual sensing paradigm. Their event-based operation, where pixels asynchronously output data only upon detecting changes in intensity, offers inherent advantages over traditional frame-based cameras. This approach reduces data redundancy and enables high temporal resolution, which makes DVS particularly suitable for dynamic and fast-changing environments [3]. Among the numerous applications benefiting from DVS technology, object detection, tracking, optical flow estimation, etc. are critical for real-time motion analysis, robotics, and autonomous navigation systems [3]. Fig. 1 provides an overview of a DVS-based system for real-time motion analysis in a robotic agent.

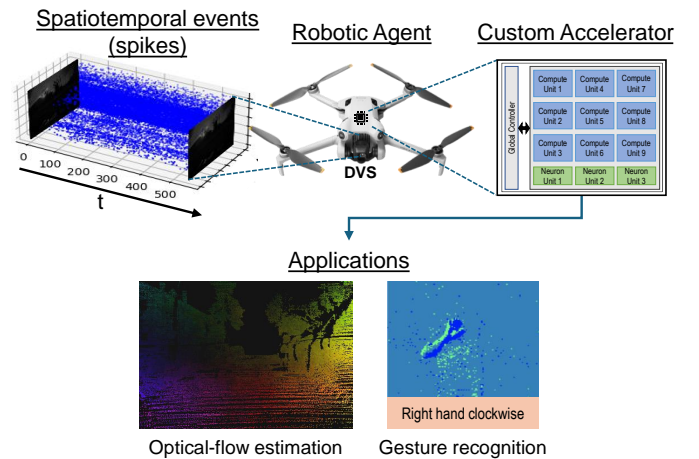


Fig. 1. A conceptual diagram showcasing the use of DVS camera and a specialized accelerator for real-time motion analysis tasks (such as optical-flow estimation) in a robotic agent.

Nevertheless, processing Dynamic Vision Sensor (DVS) data introduces unique challenges and opportunities, primarily due to its event-driven and sparse nature. Traditional Analog Neural Networks (ANNs)¹, while powerful for a wide range of applications, face difficulties fully utilizing the asynchronous event streams and precise temporal information provided by DVS data. In contrast, Spiking Neural Networks (SNNs), inspired by biological neural dynamics, inherently align with the sparse, event-driven nature of DVS data and offer a more efficient processing paradigm [4], [5].

However, traditional general-purpose computing architectures, such as CPUs and GPUs, struggle to accommodate the sparse and asynchronous nature of SNN computations [6]. Designed around synchronous data flows, they incur overheads when converting event-based data into frame-like representations. In addition, their regular memory access patterns do not align with the unpredictable dynamic computations of SNNs, leading to an underutilization of processing units during sparse computations. Therefore, there is increased interest in developing specialized accelerators tailored to the unique

¹ANN refers to standard neural networks that operate on multi-bit input and activation values (unlike spike-based digital inputs), including CNNs, MLPs, RNNs, LSTMs, etc.

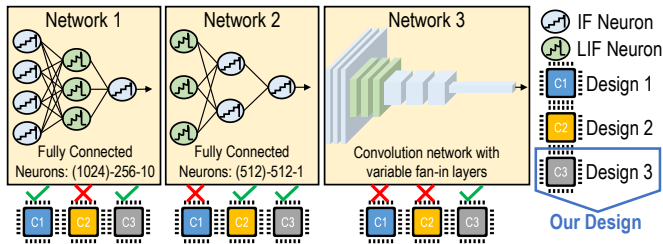


Fig. 2. Lack of reconfigurability in existing SNN architectures.

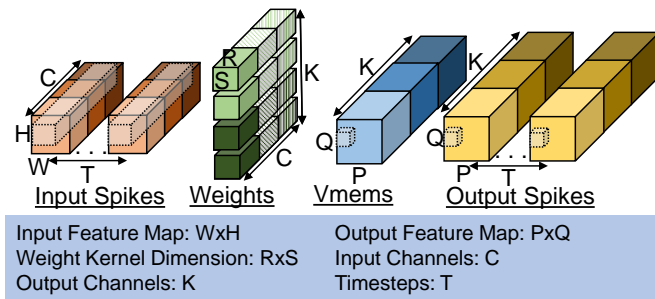


Fig. 3. An example spiking convolution layer.

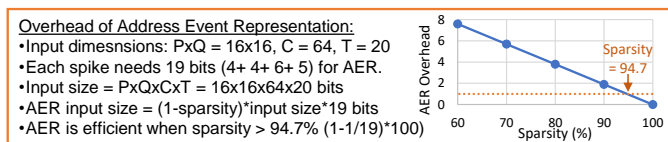
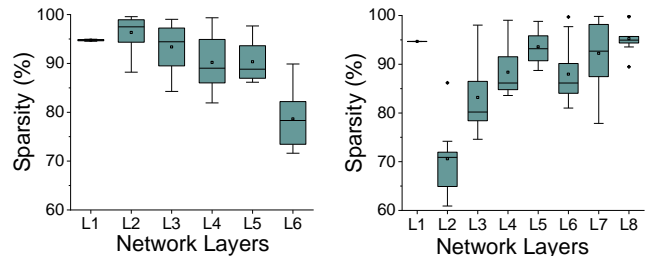


Fig. 4. Overhead of using AER for input spikes for varying input sparsity.

demands of event-based processing to maximize performance and efficiency [7]–[13].

Despite these efforts, current SNN accelerators face several limitations in terms of scalability and flexibility that hinder their widespread adoption. A key limitation among these is the lack of versatile support for diverse network architectures [9], [10], [14], [15], variable bit precision [9], [10], [14] and different neuron models [8]–[11], [15] (Fig. 2). Limitations in architectural support restrict the types of networks that can be efficiently implemented on the hardware. Furthermore, bit precision constraints hinder the exploration of accuracy and energy consumption trade-offs, and the inability to accommodate different neuron models limits the computational capabilities of SNNs on these accelerators. Additionally, many existing designs do not discuss the storage and data movement overhead of the membrane potential (Vmem) data structure. As a result, even when low precision is used for weights, high precision is used for Vmems [8], [9], [13], which can add high processing and memory overhead, particularly for layers with large output dimensions.

Finally, to achieve high efficiency, most SNN accelerators rely on sparse optimizations, such as address event representation (AER) for input spikes [9], [10]. However, AER is primarily beneficial for data structures with a high sparsity or small size (fewer data points). This leads to inconsistencies since the sparsity levels of input spikes in SNNs can vary significantly across different network architectures or even within layers of



(a) Gesture recognition (b) Optical flow estimation

Fig. 5. Variation in input sparsity across different networks and layers of the same network.

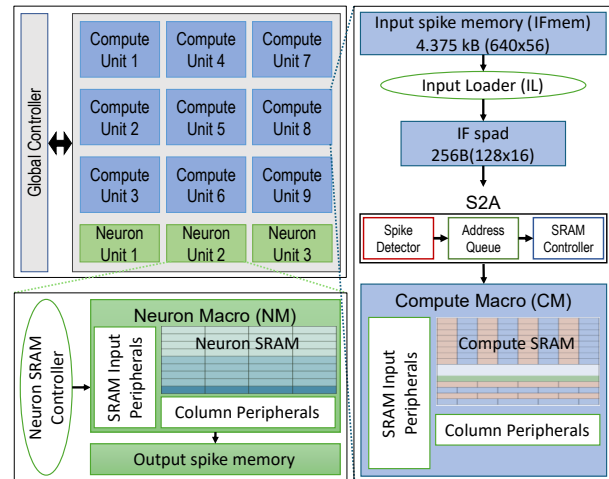


Fig. 6. Proposed SNN core architecture

the same network. Fig. 3 illustrates the various data structures in a general spiking convolution layer. Fig. 4 then highlights the overhead of using AER at different input sparsity levels for such a layer, demonstrating that AER is effective only when sparsity exceeds 94.7% in this example. Fig. 5 further reinforces our point by showcasing the variation in sparsity across layers in two SNNs designed for gesture recognition and optical flow estimation tasks. The details of these networks are presented in Section III. Notably, the sparsity of inputs for the second layer of the optical flow estimation network can be as low as 60% and never goes beyond 75% whereas, the sparsity of the next layer inputs ranges from 75% to 99%. This analysis underscores the need for SNN accelerators that can efficiently handle varying sparsity levels rather than relying solely on optimizations that are effective in specific cases but increase the overheads in other cases.

This work introduces a scalable and reconfigurable SNN inference core SpiDR, that addresses the limitations discussed above through several key strategies outlined below:

- It uses in-memory computation, reconfigurable operating modes, and timestep pipelining to efficiently support various workload sizes while minimizing weight and Vmem data movement.
- It seamlessly incorporates three weight/Vmem bit precisions (4/7, 6/11, 8/15) into the macro design, enhancing parallelism with full resource utilization, allowing a

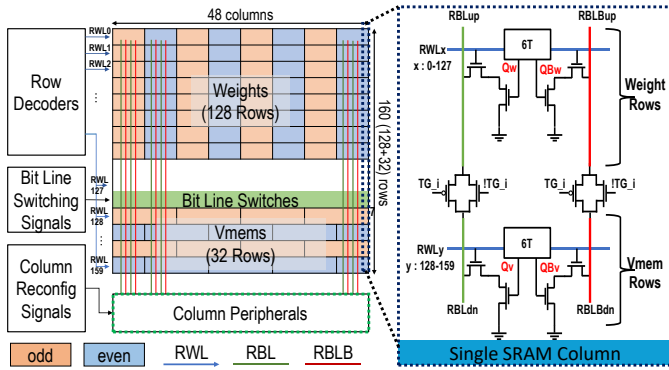


Fig. 7. Compute macro architecture.

balanced trade-off between computational accuracy and energy consumption.

- It employs a zero-skipping strategy to leverage a wide range of input sparsity, reducing energy and latency with minimal overhead.
- It uses an asynchronous handshaking mechanism to maintain the efficiency of the computation pipeline.

II. PROPOSED SNN CORE ARCHITECTURE

Fig. 6 shows the proposed SNN core with 9 compute units (CU) and 3 neuron units (NU). The compute units accumulate weights into partial Vmems based on input spike values. Each compute unit consists of an input spike memory (IFmem), input loader (IL), input scratchpad buffer (IFspad), spike-to-address converter (S2A), and a CIM compute macro (CM). The IFmem stores the input spike values in raw/uncompressed form. The input loader transfers data from IFmem to IFspad, aligning for convolution (Conv) or fully connected (FC) layer operations. The spike-to-address converter converts IFspad spikes into weight and Vmem row addresses for in-memory weight to Vmem accumulation in the compute macro. Neuron units receive partial Vmems from compute units and perform the required neuron operations (e.g. accumulation and threshold comparison for Integrate and Fire (IF) neuron) using the CIM neuron macro (NM) coordinated by a neuron SRAM controller. The following paragraphs in this section describe each of these components in detail.

A. Macro design

Fig. 7 details the compute macro, an enhanced version of the design presented in IMPULSE [16]. The core component of the macro is a 160×48 10T SRAM array, where the top 128 rows store synaptic weights, and the remaining 32 rows are used for storing partial membrane potentials (Vmems). Similar to IMPULSE, this design integrates the weight and Vmem arrays within the same SRAM structure. This co-location enables the accumulation of weights into partial Vmems directly within the memory array using some peripheral circuitry. This in-memory approach significantly reduces the energy-intensive data movement typically required between separate memory and compute units, thereby enhancing the overall efficiency of the SNN accelerator.

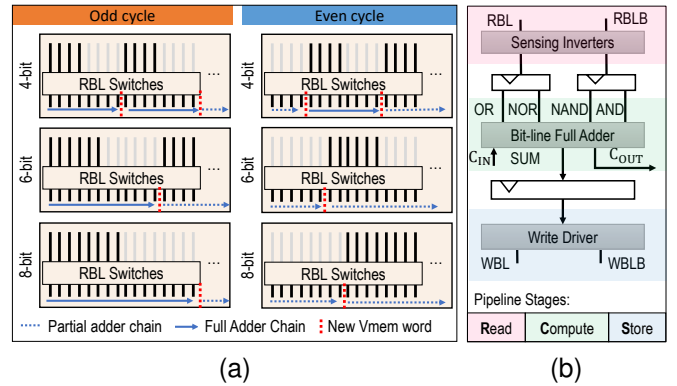


Fig. 8. (a) Variable bit precision support. (b) Column peripherals.

As multiple weights accumulate into Vmems, the precision required for Vmems is usually greater than the precision required for weights. In this work, we assume the Vmem precision (B_{Vmem}) to be roughly equal to two times the weight precision (B_{weight}), that is, $B_{Vmem} = 2 * B_{weight} - 1$. Consequently, we need two memory rows to store the Vmems corresponding to one weight row in a staggered layout. IMPULSE [16] uses an additional read word line (RWL) for each weight row to support these staggered computations. A key enhancement in our macro design is using transmission gates as read bit line (RBL) switches to connect the bit lines between weight and Vmem arrays. This modification eliminates the need for the additional RWL per weight memory row.

Moreover, this design also enables reconfigurable bit precision support. The previous macro [16] was limited to a single weight/Vmem bit precision configuration (6/11-bit) determined at design time by its dual RWL connectivity. Our compute macro offers greater flexibility by supporting multiple weight and Vmem bit precisions by changing the RBL switch connectivity and column peripheral configurations. Supported weight/Vmem bit precision configurations include 4/7-bit, 6/11-bit, and 8/15-bit, enabling the accelerator to adapt to the accuracy and efficiency requirements of different SNN workloads. The bit precision required for a particular workload can be selected as a configuration parameter before starting execution, avoiding any reconfigurability overhead. Fig. 8a shows the RBL switch and column adder chain configurations for different bit precisions and even/odd accumulation cycles. Bit lines are numbered in ascending order (0 to 47) from left to right. For a 4-bit odd cycle operation, as an example, odd weights are added to an odd Vmem row, activating RBL switches at lines (0-3), (8-11), ..., and (40-43).

The weight to Vmem accumulation operation is performed with the help of the column peripheral circuitry illustrated in Fig. 8b. Adding one row of weights to Vmems consists of three pipelined stages:

- 1) **Read (R):** One weight RWL and one Vmem RWL are activated. This generates *NOR* and *AND* outputs at RBL and RBL bar (RBLB), that are sensed using inverters and latched. Latching these outputs allows them to be used reliably in the next compute stage.
- 2) **Compute (C):** The latched outputs, along with the carry-

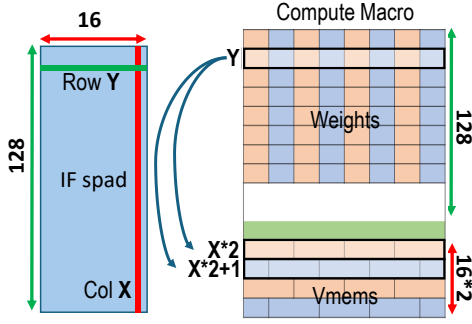


Fig. 9. Effective operations corresponding to one spike at row Y and column X in IFspad.

in (C_{IN}) bit from the adjacent column, are used to generate the SUM and carry-out (C_{OUT}) bits. A simple adder circuit performs this computation.

3) **Store (S):** The SUM bit is written to the active Vmem row.

The design of neuron macros is similar to compute macros, with a 72×48 memory array. Of these, 32 rows store partial Vmems (membrane potentials received from the compute units), another 32 store full Vmems, and the remaining rows are reserved for storing neuron model-specific parameters like thresholds and leak values.

The neuron macros support integrate-and-fire (IF) and leaky-integrate-and-fire (LIF) neuron models with soft and hard reset options following a neuron spike. The hard reset option resets the Vmem to zero, while the soft reset option subtracts the threshold voltage from the Vmem, retaining some residual potential. The choice of neuron model and reset method influences the neuron's firing dynamics and can be tailored to specific SNN tasks. To implement these reset options, the *Store* stage of the compute pipeline is augmented with conditional write logic, allowing it to perform the appropriate reset operation only when a neuron fires (i.e. generates an output spike).

Another significant difference from the IMPULSE design [16] is the separation of functionality. While IMPULSE combined weight-to-Vmem accumulation and neuron operations within a single macro, our design explicitly divides these tasks between the compute and neuron macros. This decoupling enhances the accelerator's flexibility, allowing it to handle SNNs with varying layer sizes efficiently. The reconfigurable operating modes enabled by this separation are discussed in greater detail in Section II-E.

B. Amortizing switching overhead

Fig. 9 illustrates the mapping of input spikes in the 128×16 IFspad array with respect to the weights and Vmem rows of the compute macro. Each row (Y) in the IFspad directly corresponds to a row of the weight memory and each column (X) of the IFspad is associated with two consecutive rows of the Vmem memory – an even row $X * 2$ and an odd row $X * 2 + 1$. This mapping facilitates the accumulation of weights into corresponding Vmem locations. The address of each spike

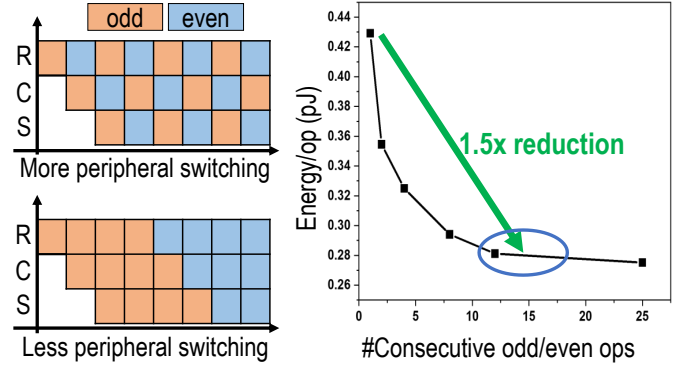


Fig. 10. Peripheral switching Overhead.

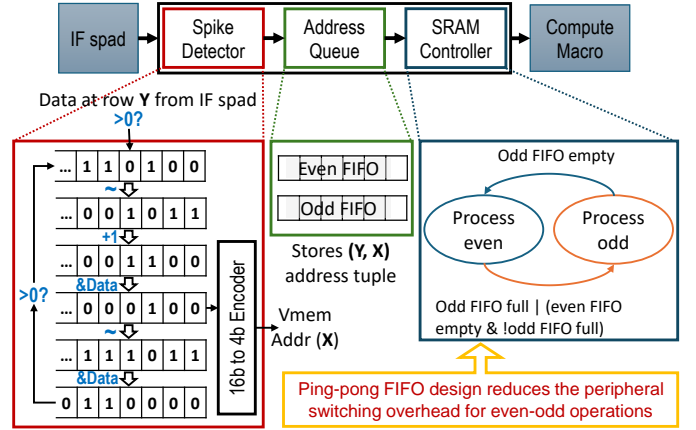


Fig. 11. Peripheral switching Overhead.

(Y, X) in the IFspad is fed to the address queue. The compute macro then performs two operations for each (Y, X) pair:

- **Even Accumulation:** The even-numbered weights from row (Y) in the weight memory are added to the values stored in the even Vmem row ($X * 2$).
- **Odd Accumulation:** The odd-numbered weights from the same row (Y) are added to the values in the odd Vmem row ($X * 2 + 1$).

A naive way would be to consecutively perform one even and one odd cycle operation. However, switching between even and odd operations requires changing the bit line switch and peripheral connectivity as shown in Fig. 8a. We studied the overhead of this continuous switching on the overall energy consumption of the compute macro (Fig. 10) and separate the even and odd operations to minimize this overhead. By performing multiple consecutive operations of the same type (even or odd), we can significantly reduce the frequency of these switches, resulting in substantial energy savings. As shown in Fig. 10, switching peripherals after 15 consecutive even or odd operations, as opposed to after every cycle, results in a $1.5\times$ reduction in energy per operation. This insight drives the design of our spike-to-address converter (S2A), ensuring that spikes are processed with optimal energy savings.

C. Spike-to-address converter (S2A)

The S2A (Fig. 11) consists of three primary components: a spike detector, an address queue, and an SRAM controller. The spike detector, a low-complexity trailing zero detector, reads and processes a row of the IFspad, representing weight address Y , and identifies the column location of the spikes, representing Vmem address (X). This address is stored in the address queue as a weight, Vmem address tuple (Y, X) . The SRAM controller reads the address tuple from the address queue and issues control signals to the compute macro to perform the accumulation operation.

The address queue is designed to minimize the even-odd operation switching as explained in Section II-B. We employ an even-odd ping-pong FIFO mechanism for the address queue. This means that after reading and processing an address tuple from the even FIFO, the same tuple is written to the odd FIFO. This mechanism strategically batches consecutive even or odd operations, as shown in Fig. 10. The SRAM controller oversees this ping-pong behavior, switching between even and odd operations only when the current FIFO is empty or the other FIFO is full. The depth of both even and odd FIFOs is set to 16, as a further increase in depth does not provide significant additional energy reduction, as evidenced by Fig. 10.

D. Input loader

We use a dual-port SRAM to implement the IFspad, allowing simultaneous read and write operations. The spike detector in the spike-to-address converter (S2A) is connected to the read port, while the input loader (IL) writes new data into the IFspad through the write port.

The CIM compute macro effectively performs a general matrix multiply (GEMM) operation. However, as input spikes are binary (0 or 1), explicit multiplication is unnecessary and can be replaced by only accumulation operations. Regardless, to perform convolution operations using the hardware capable of performing GEMM efficiently, they are first converted to a GEMM-compatible format, for example using the im2col algorithm to transform the input tensor [17], [18].

Traditionally, im2col is implemented as a software pre-processing step, requiring additional memory due to data replication. Our design uses the input loader to perform im2col directly in hardware during execution. The latency of this hardware im2col operation is hidden by exploiting the dual-port SRAM's separate read and write paths. This allows the S2A to begin reading and processing data from the IFspad as soon as the input loader has populated a few rows, rather than waiting for the entire IFspad to be filled. In addition to the im2col transformation, the input loader handles any necessary zero padding and incorporates stride values directly into the IFspad's data layout. The dataflow mapping utilized by the input loader is detailed in the following section.

E. Reconfigurable operating modes

Each compute macro in our accelerator computes partial Vmems for multiple output neurons concurrently. We employ a weight-stationary mapping strategy, common for in-memory computing designs, where different output channels of a Conv

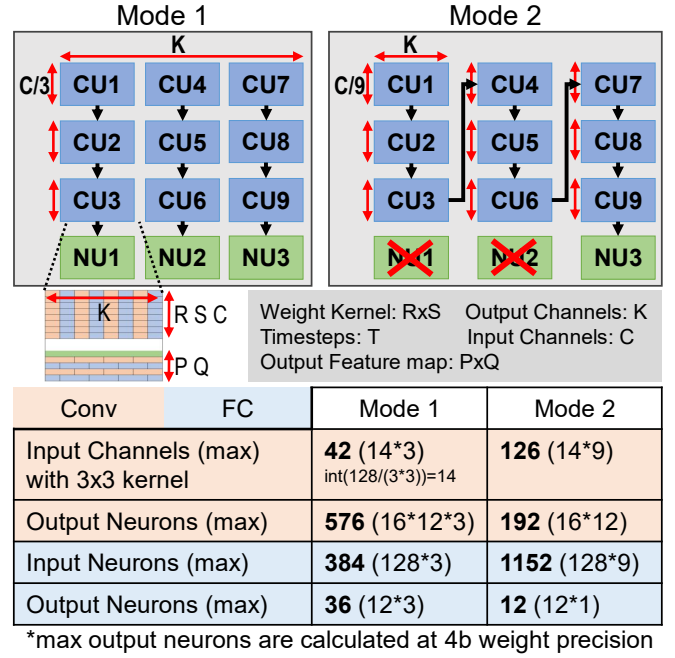


Fig. 12. Reconfigurable operating modes.

layer (K) or different output neurons for an FC layer are mapped along the column dimension of the macro. The spatial input dimensions (R, S, C), which represent the receptive field over which a partial Vmem is accumulated, are mapped across the rows of the compute macro. For a 4-bit weight precision, each row can store weights corresponding to 12 i.e. $(48/4)$ output neurons. One input spike corresponds to the weight-to-Vmem accumulation of these 12 neurons in two cycles (one even and one odd). To utilize the weight reuse in convolution operations, there are 32 Vmem rows per macro. Only 2 out of these 32 rows are used for FC layers because there is no weight reuse. For a weight bit precision of W_b , the number of output neurons per macro is represented by,

$$\# \text{ output neurons per macro} = \frac{48}{W_b} * 16 \quad (1)$$

where, 48 corresponds to the column dimension of the SRAM array, and 16 represents the effective number of Vmem rows $(32/2)$ as there are two rows for a weight row.

Our design limits the movement of partial Vmem values within the core. This is achieved by mapping the entire input fan-in ($R \times S \times C$ for Conv layers or the number of input neurons for FC layers) onto the core itself. This mapping is facilitated by two operating modes, illustrated in Fig. 12:

- **Mode 1:** This mode is used for layers with a smaller input fan-in ($< 128 \times 3$), where the spatial input dimensions can fit entirely within three compute macros. Mode 1 uses three parallel pipelines each with three compute and one neuron macro to enable simultaneous computation of partial Vmems for more output channels.
- **Mode 2:** In contrast, mode 2 is used for layers with larger input fan-ins ($> 128 \times 3$ and $< 128 \times 9$). In this mode, partial Vmems are accumulated across 9 compute macros,

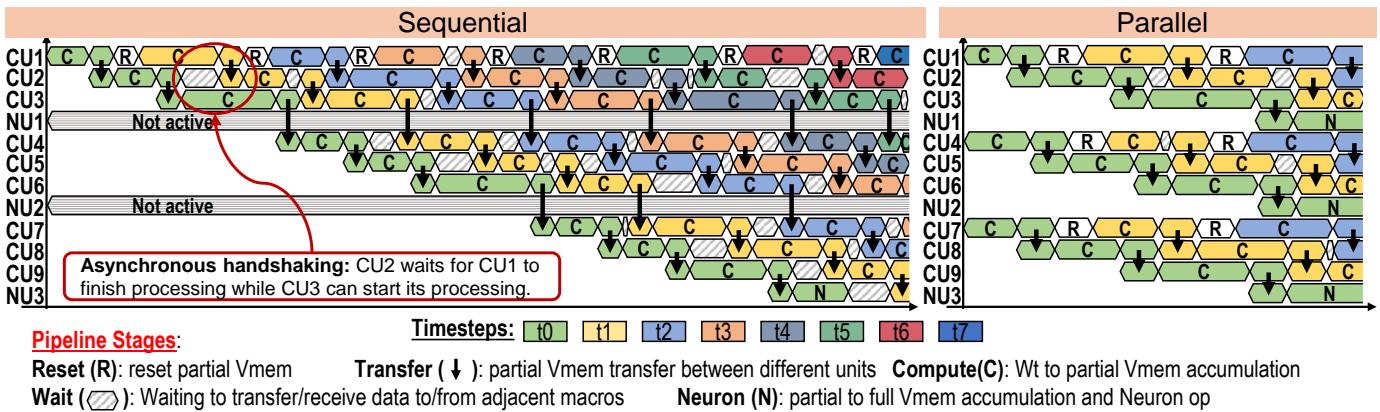


Fig. 13. Timestep pipelining with asynchronous handshaking.

and only 1 neuron macro is utilized. This mode sacrifices some parallelism but reduces data movement compared to an alternative where partial Vmems are stored off-chip and need to be fetched for every timestep.

The number of output channels processed in parallel by these modes is given by,

$$3 * \frac{48}{W_b} (\text{Mode 1}) \text{ or } \frac{48}{W_b} (\text{Mode 2}) \quad (2)$$

Our layer mapping strategy, coupled with the adaptable operating modes makes our design easily scalable to a multi-core architecture where each core can process independent output neurons in parallel, increasing throughput without additional data movement. The input loader uses this mapping information to load data into the IFspad for each macro.

F. Timestep pipelining

We pipelined the timesteps across compute and neuron units as demonstrated by Fig. 13. Each neuron macro takes a fixed number of cycles which is given by,

$$\# \text{ cycles} = 2 * 32 + 2 = 66; \quad (3)$$

where $32 * 2$ represents the partial-to-full Vmem accumulation and threshold comparison cycles and 2 additional cycles are for filling and emptying the column peripheral pipeline. However, the execution time of each compute macro depends on the sparsity of spikes in its IFspad. Therefore, a pipeline with constant execution times will need to assume the worst-case sparsity and will adversely affect the latency and throughput of the design. Instead, to maintain high computational efficiency despite the variable execution times, we introduce an asynchronous handshaking mechanism to coordinate computations ensuring that the delays are incurred only due to data dependence, and each unit can start computation as soon as it receives the required data.

As illustrated in Fig. 13, after the compute unit CU2 processes partial Vmems for timestep t1, it forwards them to CU3 and waits to receive data from CU1. CU3 can start processing its partial Vmems for timestep t1 during this period. Meanwhile, after completing its computations for timestep t2 CU1 will send its data to CU2. This dynamic, asynchronous

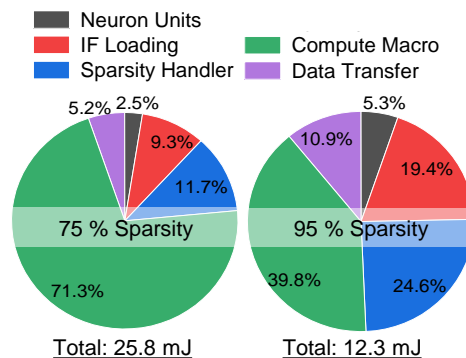


Fig. 14. Peripheral switching Overhead.

coordination ensures efficient utilization of resources and minimizes the computational pipeline stalls.

To further optimize this pipelined approach, the input channels are evenly distributed among the compute macros, as shown in Fig. 12, utilizing the same number of rows in each macro. This balanced distribution minimizes the potential waiting times, as the only factor responsible for the variable execution time of each macro is the variation in spike density and not the number of valid data rows.

III. EXPERIMENTS AND RESULTS

Fig. 14 presents a breakdown of the energy consumption for each component within the SNN core at two input sparsity levels: 75% and 95%. Notably, the CIM macros (Compute Macro + Neuron Units), responsible for weight-to-Vmem accumulation, and neuron operations are the dominant energy consumers both at a moderate input sparsity of 75% and a very high input sparsity of 95%. This observation highlights the efficiency of our design, as the energy overhead associated with control logic and peripheral circuitry does not overpower the energy required for actual computations. However, the overall energy consumption of the SNN core is significantly influenced by input sparsity, decreasing by more than 50% when the input sparsity increases from 75% to 95%, highlighting the importance of exploiting input sparsity in SNNs.

Furthermore, the energy consumed by data movement, a critical bottleneck in many traditional architectures, constitutes

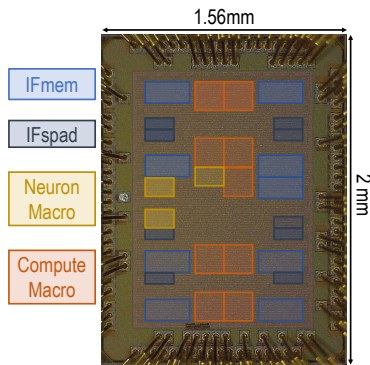


Fig. 15. Die Micrograph.

TABLE I
CHIP SUMMARY

Technology	65 nm CMOS					
Die size	1.56mm x 2mm					
On chip SRAM	Total: 52.08 kB IMC Macros: 9.7 kB Excluding input spike memories*: 12.7 kB					
Supply Voltage	0.9V - 1.2V					
Frequency	50MHz - 150MHz					
Weight/Vmem Precision	4/7-bit, 6/11-bit, 8/15-bit					
	@50MHz, 0.9V		@150MHz, 1V			
Power Consumption (mW)	4.9		18			
Weight Precision	4b	6b	8b	4b	6b	8b
Energy Efficiency (TOPS/W) @95% sparsity	5	3.34	2.5	4.09	2.73	2.04
Throughput (GOPS) @95% sparsity	24.54	16.36	12.27	73.59	49.06	36.80

*Large input spike memories are not required if the core is used as part of a larger system and data is streamed in continuously.

only a small fraction of the total energy in our design. This can be attributed to processing in-memory and our design’s optimized dataflow, which restricts data movement. Moreover, these trends will be consistent for different layer sizes as a result of our reconfigurable operating modes.

Fig. 15 shows the die micrograph of the proposed SNN core and Table I provides a comprehensive summary of its specifications. Fabricated using 65 nm CMOS technology, the chip occupies an area of 3.12 mm² including the I/O pads. It features a total on-chip SRAM of 52.08 kB, with 9.7 kB allocated to IMC macros and 39.38 kB allocated to the input memories (IFmem). We kept our IFmems large to test the functionality and fit the inputs corresponding to large layers on-chip. In a more practical system, where the IFmems can be written in parallel to the operations, or when this SNN core is used as a part of a larger system, the IFmem size can be reduced significantly as we do not need to store all the inputs at the same time on-chip. The chip operates within a voltage range of 0.9 V to 1.2 V and a frequency range of 50 MHz to 150 MHz. It consumes 4.9 mW power at 50 MHz and 0.9 V, and 18 mW power at 150 MHz and 1 V. The chip’s energy efficiency, measured in Tera operations per second per watt (TOPS/W), varies with weight precision and sparsity levels, reaching up to 5 TOPS/W at 4-bit weight precision and 95% sparsity. Its throughput, measured in Giga operations per second (GOPS), peaks at 73.59 GOPS at 4-bit weight precision, 150MHz, and 95% sparsity.

TABLE II
NETWORK DETAILS

Application	Input size	Timesteps	Input layer	Intermediate layers	Output layer
Optical flow estimation	288x384	10	Conv (2,32)	6*Conv (32,32)	Conv (32,2)
Gesture recognition ^a	64x64	20	Conv (2,16)	4*Conv (16,16)	FC (64,11)

Conv (Input,Output Channels), FC (Input,Output Neurons)

^a2x2 maxpool with stride 2 after every two intermed. conv layers.

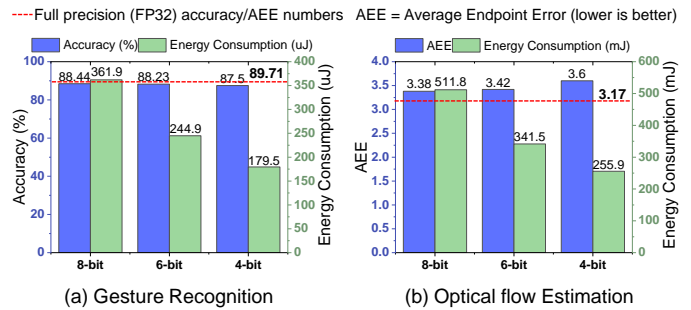


Fig. 16. Accuracy and energy consumption trade-off at different weight precisions for gesture recognition and optical flow estimation.

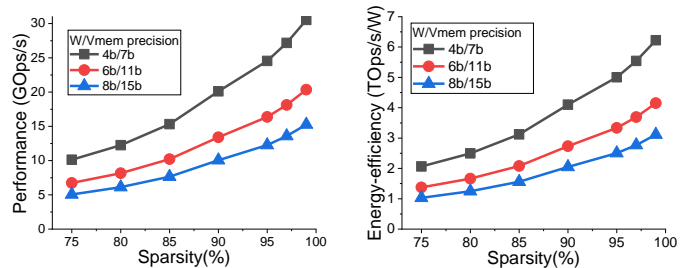


Fig. 17. Peak performance and energy efficiency trend with changing sparsity and bit precision

We evaluate the SNN core on two applications: hand gesture recognition on the IBM DVS gestures dataset [19] and optical flow estimation on the DSEC flow dataset [20]. Table II provides detailed information on the network architectures employed for each task. Fig. 16 and Fig. 17 present the measured results of our chip. The energy-accuracy trade-off at varying bit precision is shown in Fig. 16 at 50 MHz and 0.9 V. It is crucial to note that since this is a digital CIM design, there is no loss in accuracy at hardware implementation. Average endpoint error (AEE) is commonly used as a performance metric for optical flow estimation [21] as opposed to accuracy.

Fig. 17 shows the trend for peak performance (GOPS) and energy efficiency (TOPS/W) as a function of input sparsity and weight precision. For instance, there is a 2× improvement in throughput when the precision changes from 8-bit to 4-bit at the same sparsity or when the sparsity changes from 80% to 95% for 4-bit weight precision.

IV. DISCUSSION

Table III compares SpiDR with contemporary digital SNN accelerators. Although asynchronous designs with fixed network architectures [9], [10], [14] consume very low power

TABLE III
COMPARISON TABLE

Parameter	SpiDR (This Work)	C-DNN ISSCC'23 [8]	ANP-I ISSCC'23 [9]	Reck-On ISSCC'22 [10]	μ Brain Frontiers'21 [14]	SD Training ISSCC'19 [15]
Technology	65 nm CMOS	28nm CMOS	28nm CMOS	28nm FDSOI	40nm CMOS	65 nm CMOS
Supply (V)	0.9 - 1.2	0.7 - 1.1	0.56 - 0.9	0.5 - 0.8	1.1	0.8
Freq. (MHz)	50 - 150	50 - 200	40 - 210	13-115	-	20
Area⁺ (mm²)	3.12	20.25	1.63	0.87	2.82	10.08(core)
Target Domain	SNN	ANN/SNN	SNN	Spiking RNN	SNN	SNN
Neuron Model	Flexible	Fixed	Fixed	Fixed	Flexible ¹	Fixed
Neurons	inp 1152 ^a op 576 ^b	op: 2048 ^c	(1024)-512-10	(256)-256-16	(256)-64-16	2x200(hidden)
Compute type	Digital CIM	Digital	Async. Digital	Async Digital	Async Digital	Digital
Weight Prec.	4 / 6 / 8	4/8	hidden: 8, op: 10	8	4	-
Vmem Prec.	7 / 11 / 15	-	-	16	7	8
Energy Eff. [TOPS/W] (default)	4b wt: 5 (26.95) ^d 6b wt: 3.34 (18) ^d 8b wt: 2.5 (13.5) ^d @50MHz, 0.9V	CIFAR10: 63.3 ^e ImageNet: 20.8 ^e @50MHz, 0.7V	1.5 pJ/SOP @40MHz, 0.56V	5.3 pJ/SOP @13MHz, 0.5V	MNIST 308nJ/prediction (160nJ/prediction) ^d @1.1V	3.42 (18.43) ^d @20MHz 0.8V
Tasks and Datasets	IBM DVS gest. classific. Optical flow estimation on DSEC-flow	Image classific. on CIFAR-10/100 and ImageNet	MNIST classific. IBM DVS gesture classific. Keyword spotting (N- TIDIGIT, SeNic)	IBM DVS gesture classific. Keyword spotting (Spiking Heidelberg Digits) Navigation (delayed cue integration)	MNIST classific. Radar hand gest. classif. (customized dataset)	MNIST classif.
Reconfigurable Network Arch.	Yes ^f	Yes ^g	No	No	No	No
Modified Training	No	Yes	Yes	Yes	No	Yes
Sparsity Support	Supports unstructured input sparsity	^g Spiking core used when sparsity>97.7%	Yes (event-driven)	Yes (event-driven)	Yes (event-driven)	Yes (propagate only spikes)

⁺ die area as majority of the other works report only die area, ^amax input neurons when processing FC in mode 2,

^bmax output neurons when processing conv in mode 1, ^c4 clusters*8 snn cores*64 neurons per core,

^dscaled to 28nm for comparison with other accelerators assuming $energy \propto tech^2$, ^eonly SNN processing numbers,

^fhas two operating modes to trade-off fan-in with fan-out depending on application requirement,

^geach layer's mapping is decided based on sparsity, ¹supports IF but LIF can be used with an external clock

for specific applications, their lack of scalability and reconfigurability makes them unsuitable for a wide range of other applications. In contrast, SpiDR offers advanced dataflow and reconfigurability, catering to a wide range of SNN applications. Additionally, hybrid designs are mainly suitable for applications with analog inputs where ANNs outperform SNNs in accuracy [8], [13], while for dynamic tasks such as optical flow estimation, SNNs outperform ANNs [21] and our design targets these applications. Moreover, our design does not require any modified training methodology and can adapt to a variety of workload specifications.

A parallel research direction to this work is developing analog CIM architectures [11], [13] for high throughput and energy efficiency using CMOS and post-CMOS technologies such as memristors. However, analog CIM needs efficient mechanisms to address various non-idealities. Moreover, using ANNs and SNNs to complement each other for various robotic applications is another compelling area of research [12], [22]. Authors in [12] not only combine ANNs and SNNs but also use both RRAM CIM and SRAM CNM for real-time target identification and tracking. Future research directions include developing heterogeneous systems that integrate mul-

iple specialized yet reconfigurable architectures to handle diverse computational tasks in real time, adapting to ever-changing algorithmic demands. Concurrently, creating more sophisticated algorithms to leverage the full potential of such reconfigurable heterogeneous hardware platforms can pave the way for highly efficient designs.

V. CONCLUSION

This paper presents a scalable and reconfigurable digital CIM SNN accelerator SpiDR for dynamic vision tasks such as optical-flow estimation. SpiDR introduces a set of key features, including in-memory computations, reconfigurable operating modes, multi-bit precision support, a zero-skipping mechanism for sparse inputs, and an asynchronous handshaking mechanism. These features enable SpiDR to adapt to different workloads with varying neuron models, bit precisions, and network architectures while minimizing data movement and energy consumption. SpiDR was fabricated in TSMC 65 nm CMOS LP technology and demonstrates performance competitive to other digital SNN accelerators proposed in the recent literature even with advanced reconfigurability. It achieves an energy efficiency of up to 5 TOPS/W at an input sparsity of 95%, weight precision of 4 bits, and Vmem precision of 7 bits.

REFERENCES

- [1] P. Lichtsteiner, C. Posch, and T. Delbruck, "A 128×128 120 db 13 μ s latency asynchronous temporal contrast vision sensor," *IEEE journal of solid-state circuits*, vol. 43, no. 2, pp. 566–576, 2008.
- [2] C. Brandli, R. Berner, M. Yang, S.-C. Liu, and T. Delbruck, "A 240×180 130 db 3 μ s latency global shutter spatiotemporal vision sensor," *IEEE Journal of Solid-State Circuits*, vol. 49, no. 10, pp. 2333–2341, 2014.
- [3] G. Gallego, T. Delbrück, G. Orchard, C. Bartolozzi, B. Taba, A. Censi, S. Leutenegger, A. J. Davison, J. Conradt, K. Daniilidis *et al.*, "Event-based vision: A survey," *IEEE transactions on pattern analysis and machine intelligence*, vol. 44, no. 1, pp. 154–180, 2020.
- [4] W. Maass, "Networks of spiking neurons: the third generation of neural network models," *Neural networks*, vol. 10, no. 9, pp. 1659–1671, 1997.
- [5] A. K. Kosta and K. Roy, "Adaptive-spikenet: Event-based optical flow estimation using spiking neural networks with learnable neuronal dynamics," in *2023 IEEE International Conference on Robotics and Automation (ICRA)*. IEEE, 2023, pp. 6021–6027.
- [6] L. Parker, F. Chance, and S. Cardwell, "Benchmarking a bio-inspired snn on a neuromorphic system," in *Proceedings of the 2022 Annual Neuro-Inspired Computational Elements Conference*, 2022, pp. 63–66.
- [7] A. Basu, L. Deng, C. Frenkel, and X. Zhang, "Spiking neural network integrated circuits: A review of trends and future directions," in *2022 IEEE Custom Integrated Circuits Conference (CICC)*. IEEE, 2022, pp. 1–8.
- [8] S. Kim, S. Kim, S. Hong, S. Kim, D. Han, J. Choi, and H.-J. Yoo, "C-dnn: An energy-efficient complementary deep-neural-network processor with heterogeneous cnn/snn core architecture," *IEEE Journal of Solid-State Circuits*, 2023.
- [9] J. Zhang, D. Huo, J. Zhang, C. Qian, Q. Liu, L. Pan, Z. Wang, N. Qiao, K.-T. Tang, and H. Chen, "22.6 anp-i: A 28nm 1.5 pj/sop asynchronous spiking neural network processor enabling sub-0.1 μ j/sample on-chip learning for edge-ai applications," in *2023 IEEE International Solid-State Circuits Conference (ISSCC)*. IEEE, 2023, pp. 21–23.
- [10] C. Frenkel and G. Indiveri, "Reckon: A 28nm sub-mm² task-agnostic spiking recurrent neural network processor enabling on-chip learning over second-long timescales," in *2022 IEEE International Solid-State Circuits Conference (ISSCC)*, vol. 65. IEEE, 2022, pp. 1–3.
- [11] S. Kim, S. Kim, S. Um, S. Kim, K. Kim, and H.-J. Yoo, "Neuro-cim: A 310.4 tops/w neuromorphic computing-in-memory processor with low w/bl activity and digital-analog mixed-mode neuron firing," in *2022 IEEE Symposium on VLSI Technology and Circuits (VLSI Technology and Circuits)*. IEEE, 2022, pp. 38–39.
- [12] M. Chang, A. S. Lele, S. D. Spetalnick, B. Crafton, S. Konno, Z. Wan, A. Bhat, W.-S. Khwa, Y.-D. Chih, M.-F. Chang *et al.*, "A 73.53 tops/w 14.74 tops heterogeneous rram in-memory and sram near-memory soc for hybrid frame and event-based target tracking," in *2023 IEEE International Solid-State Circuits Conference (ISSCC)*. IEEE, 2023, pp. 426–428.
- [13] Y. Liu, Z. Chen, Z. Wang, W. Zhao, W. He, J. Zhu, O. Wang, N. Zhang, T. Jia, Y. Ma *et al.*, "Aa 22nm 0.43 pj/sop sparsity-aware in-memory neuromorphic computing system with hybrid spiking and artificial neural network and configurable topology," in *2023 IEEE Custom Integrated Circuits Conference (CICC)*. IEEE, 2023, pp. 1–2.
- [14] J. Stuijij, M. Sifalakis, A. Yousefzadeh, and F. Corradi, " μ brain: An event-driven and fully synthesizable architecture for spiking neural networks," *Frontiers in neuroscience*, vol. 15, p. 664208, 2021.
- [15] J. Park, J. Lee, and D. Jeon, "7.6 a 65nm 236.5 nj/classification neuromorphic processor with 7.5% energy overhead on-chip learning using direct spike-only feedback," in *2019 IEEE International Solid-State Circuits Conference-(ISSCC)*. IEEE, 2019, pp. 140–142.
- [16] A. Agrawal, M. Ali, M. Koo, N. Rathi, A. Jaiswal, and K. Roy, "Impulse: A 65-nm digital compute-in-memory macro with fused weights and membrane potential for spike-based sequential learning tasks," *IEEE Solid-State Circuits Letters*, vol. 4, pp. 137–140, 2021.
- [17] V. Sze, Y.-H. Chen, T.-J. Yang, and J. S. Emer, "Efficient processing of deep neural networks: A tutorial and survey," *Proceedings of the IEEE*, vol. 105, no. 12, pp. 2295–2329, 2017.
- [18] S. Chetlur, C. Woolley, P. Vandermersch, J. Cohen, J. Tran, B. Catanzaro, and E. Shelhamer, "cudnn: Efficient primitives for deep learning," *arXiv preprint arXiv:1410.0759*, 2014.
- [19] A. Amir, B. Taba, D. Berg, T. Melano, J. McKinstry, C. Di Nolfo, T. Nayak, A. Andreopoulos, G. Garreau, M. Mendoza *et al.*, "A low power, fully event-based gesture recognition system," in *Proceedings of the IEEE conference on computer vision and pattern recognition*, 2017, pp. 7243–7252.
- [20] M. Gehrig, W. Aarents, D. Gehrig, and D. Scaramuzza, "Dsec: A stereo event camera dataset for driving scenarios," *IEEE Robotics and Automation Letters*, vol. 6, no. 3, pp. 4947–4954, 2021.
- [21] S. Negi, D. Sharma, A. K. Kosta, and K. Roy, "Best of both worlds: Hybrid snn-ann architecture for event-based optical flow estimation," *arXiv preprint arXiv:2306.02960*, 2023.
- [22] A. R. Vidal, H. Rebecq, T. Horstschaefer, and D. Scaramuzza, "Ultimate slam? combining events, images, and imu for robust visual slam in hdr and high-speed scenarios," *IEEE Robotics and Automation Letters*, vol. 3, no. 2, pp. 994–1001, 2018.